

# Performance monitoring techniques for semiconductor pixel detectors in long-term operations\*

Huai-Zhong Gao,<sup>1,2,3,4,5</sup> Xu-Tao Zheng,<sup>1,2,†</sup> Jia-Xing Wen,<sup>6,‡</sup> Qi-Dong Wang,<sup>1,2,3,4,5</sup> Ge Ma,<sup>1,2</sup> Yu-Ge Zhang,<sup>1,2</sup> Xiao-Fan Pan,<sup>1,2</sup> Chen Li,<sup>1,2</sup> Ming Zeng,<sup>1,2</sup> Ming-Hai Yu,<sup>6</sup> Si-Xin Wu,<sup>6</sup> Yue Yang,<sup>6</sup> Zong-Qing Zhao,<sup>6</sup> Li-Ye Liu,<sup>3,4,5</sup> Heng-Guan Yi,<sup>3,4,5</sup> and San-Qiang Xia<sup>3,4,5</sup>

<sup>1</sup>Key Laboratory of Particle and Radiation Imaging (Tsinghua University), Ministry of Education, Beijing 100084, China

<sup>2</sup>Department of Engineering Physics, Tsinghua University, Beijing 100084, China

<sup>3</sup>China Institute for radiation protection, Shanxi, Taiyuan 030006, China

<sup>4</sup>Shanxi Provincial Key Laboratory for Radiation Safety and Protection, Shanxi, Taiyuan 030006, China

<sup>5</sup>CNNC Key Laboratory for Radiation Protection Technology, Shanxi, Taiyuan 030006, China

<sup>6</sup>National Key Laboratory of Plasma Physics, Laser Fusion Research Center, CAEP, Mianyang 621900, Sichuan, China

Semiconductor pixel detectors are widely used in various applications, many of which require sustained stability of the detector performance over extended periods of operations. However, the presence of irreversible and temporary degradations can impact the performance of the detector over extended periods of use. Thus, maintaining continual monitoring of the detector performance that is susceptible to degradation effects become necessary. This paper presents a cost-effective examination procedure for real-time monitoring and regular inspections of pixel detectors during prolonged operations. The real-time monitoring method monitors the charge drifting process without introducing additional background by utilizing the cosmic muons to identify temporary effects caused by shifts in operating conditions, such as ambient temperature fluctuations. On the other hand, the offline inspection regularly evaluates the per-pixel spectral characteristics including baseline and gain using simple radioactive sources to evaluate the extent of irreversible degradation. The monitoring procedure is validated on a Timepix3 detector equipped with a CdTe sensor which proves its effectiveness.

Keywords: Semiconductor pixel detectors, Real-time performance monitoring, Regular performance inspection, Performance monitoring with muons

## I. INTRODUCTION

Semiconductor pixel detectors are widely utilized in diverse fields such as medical imaging [1, 2], electron microscopy [3, 4], radiotherapy [5, 6], and scientific research, including particle accelerator experiments [7], low-background studies like the search for  $0\nu\beta\beta$  decay [8] as well as high flux studies like diagnostic systems in fusion devices [9–11]. In some applications like the low-background experiments, continuous data acquisition is required, which necessitates prolonged stability of the detector [8]. Applications for medical and scientific purposes like medical imaging and electron microscopy may not require constant operation, but still demand consistent detector performance over extended periods of usage [12–15]. However, prolonged usage exposes detectors to temporary and even irreversible performance degradation. The temporary performance degradation can be caused by variations in the operating conditions such as changes in the environment temperature. This type of degradation can affect the charge collection process in detectors with sensor materials such as silicon [16], CdTe [42] as well as GaAs [17] and result in fluctuations of the detector response. Additionally, intrinsic properties of the sensor material, such as polarization effect in CdTe detectors [33–39], can also cause distortions in the captured physical signals. Both of the aforementioned cases can potentially yield anomalous

data. On the other hand, irreversible performance degradation can result from aging effects, such as interface deterioration in CdZnTe detectors [32] and radiation-induced damage caused by either accumulated exposure or high flux irradiation. Such damage typically occurs when the integrated particle flux reaches  $10^{13} – 10^{16}$  p/cm<sup>2</sup> for proton irradiation [18, 21, 22, 25, 28], photon irradiation [19, 20, 24, 26, 27, 30] and electron irradiation [27, 29]. It can lead to distorted and reduced charge collection efficiency (CCE) as well as increased leakage current in silicon [18, 21, 22, 30], CdTe [20], CdZnTe [20, 23–26], GaAs [27–29] and SiC [19, 30] detectors. The cumulative impact of these aging effects over time results in deteriorating detector performance and eventually leads to signal distortion and degradation in the measured data. In scenarios with high particle flux, such as the diagnostic systems in fusion devices [9–11], aging effects due to radiation damage can cause the detectors to cease operation, leading to a complete loss of data, or create unwanted background data [9]. Therefore, continuous monitoring of the detector performance and stability during long-term operations is essential. To identify the temporary performance degradation, it is necessary to monitor the key aspects of detector performance, namely the parameters associated with the charge collection process, in real-time. Once the temporary shifts in the detector response are detected, appropriate measures such as temperature stabilization can be taken to mitigate the changes effectively. On the other hand, the extent of irreversible degradation should be assessed via regular evaluations of the detector performance, encompassing factors like leakage current and CCE that can affect the operating parameters such as baseline [31] and gain. Subsequently, energy calibration and gain correction may be essential to sustain the functionality of the detectors. In cases where the degra-

\* Supported by the National Natural Science Foundation of China (Grant No. 12305228)

† Co-corresponding author, zhengxt18@mails.tsinghua.edu.cn

‡ Corresponding author, wenjx13@mail.tsinghua.org.cn

tion exceeds permissible levels, replacement of the detectors would be needed. These performance monitoring procedures are helpful in maintaining data integrity and avoiding the inaccuracies beforehand, particularly in applications like diagnostic systems in fusion devices where the measurements are costly and lengthy, and the replacement of detectors must be performed offline. There are existing methods to calibrate the aforementioned aspects of detector performance susceptible to degradation. Parameters related to the charge collection process can be determined utilizing energetic charged particles, such as pions generated by accelerators [43] and cosmic muons [4, 44]. However, these measurements are typically performed outside the regular operational periods. Such measurements can be more advantageous if they can be performed in real time since the charge collection process is primarily affected by the temporary degradation that may vary over time. Additionally, the effects induced by irreversible degradation, namely increased leakage current and reduced CCE, leads to elevated electronic noise levels, raised detector baseline and reduced detector gain. Thus, identifying these effects involve offline assessment of the detector baseline and gain. While both procedures are currently well-established, the gain assessment often entails the use of radiation apparatus such as X-ray devices. This poses challenges for regular inspections, especially in industrial and medical settings where numerous detectors are deployed. In order to overcome the limitations with the existing evaluation methods in identifying performance degradations over extended periods of operation, it is necessary to implement a cost-effective approach that integrates online monitoring with regular offline inspections. This approach is crucial for the timely detection of performance deterioration and early warning of potential detector failures or anomalous data.

This paper introduces a low-cost detector monitoring procedure to facilitate regular assessments of the detector performance. The procedure utilizes cosmic muons to monitor the charge collection process in real time, alongside periodic inspections using easily procurable low-activity calibration sources to assess the characteristics susceptible to irreversible degradation. This approach can be used to effectively monitor the detector performance that can be impacted by temporary and irreversible degradation during long-term operations. The proposed method is validated on MiniPIX TPX3, a Timepix3 detector manufactured by ADVACAM. The detector is equipped with a 1 mm-thick CdTe sensor which has an active area measuring  $14.08 \times 14.08 \text{ mm}^2$  and a total of  $256 \times 256$  pixels with a pixel size of  $55 \mu\text{m}$ . A schematic of the sensor structure is given in Fig. 1(a).

107

## II. PERFORMANCE MONITORING METHODS

The proposed performance monitoring procedure comprises two types of measurements: real-time monitoring and offline inspection. The real-time monitoring focuses on monitoring changes in the charge collection process to identify the temporary degradation. This approach is developed based on

the previously reported charge carrier drift time calibration method utilizing cosmic muons [4, 44]. This monitoring procedure can be conducted concurrently with normal operation without the need for additional radioactive sources, thereby avoiding the introduction of extra background noise. On the other hand, the offline inspection is designed to evaluate the detector characteristics, such as baseline and gain, that are susceptible to irreversible degradation. Unlike conventional methods that are reliant on radiation apparatus, this method only requires simple, low-activity radioactive sources and can be implemented cost-effectively. It is well-suited for applications in the medical and industrial sectors that involve a large number of detectors. Detailed descriptions of the performance monitoring procedure are provided in the following sections.

### A. Real-time monitoring of charge collection process

The real-time monitoring process is specifically designed to monitor the distribution of the internal electric field and assess the behaviour of charge carriers as they drift, providing insights into the charge collection efficiency within the sensor. As discussed in the previous section, this procedure relies solely on cosmic muons, which tend to follow straight trajectories within the sensor. This approach has been documented in previous studies [4, 43, 44]. Here, we present a comprehensive outline of the data selection and parameter extraction procedures.

Unlike previously proposed calibration method that requires dedicated cosmic muon measurements, our method utilizes the data gathered during normal operation to identify cosmic muon tracks for analysis. This data collection method allows for continuous monitoring of the detector response to detect time-varying changes by examining the data from any designated time frame. This endows the proposed method with real-time monitoring capabilities and enhanced flexibility. On the other hand, cosmic muons are also well-suited as a persistently existing calibration source for the continuous performance monitoring during long-term operations without introducing additional background, particularly in scenarios requiring a significant number of detectors. Following the data selection stage, the muon tracks are fitted to establish the relationship between the drift time of the charge carriers collected at the pixel electrode (electrons for detectors with pixel anodes or holes for detectors with pixel cathodes, referred to as “collected charge carrier” hereafter) and the depth of interaction. This correlation is instrumental in order to derive the electric field distribution. By leveraging the linear trajectories of energetic charged particles that traverse the full sensor thickness, these tracks can be reconstructed geometrically. This enables the establishment of a connection between the measured charge carrier drift time and the reconstructed interaction depth. The drift velocity of charge carriers at a specific depth  $z$  is given by

$$v(z) = -\frac{dz}{dt} = \mu E_{\text{int}}(z), \quad (1)$$

where  $\mu$  is the mobility of the charge carrier and  $E_{\text{int}}(z)$  is the internal electric field at the given depth. By integrating Eq. (1) the correspondence between interaction depth  $z_0$  and drift time  $t_0$  can be derived,

$$t_0 = \int_0^{z_0} \frac{dz}{\mu E_{\text{int}}(z)}, \quad (2)$$

which can be fitted using the reconstructed linear tracks of charged particles and thus the parameters of the internal electric field can be obtained. To identify these linear tracks from the data collected, an initial 2-dimensional linear fit is applied to the tracks along the pixel plane. Tracks with significant fit errors, such as the ones generated by non-muon particles and the ones with branches diverging from the primary particle tracks that are often generated by the secondary particles like  $\delta$ -electrons ( $\delta$ -rays), are excluded from further analysis. Subsequently, a 3-dimensional linear fit is conducted on the remaining tracks to eliminate any outlying pixel signals from the primary tracks. The tracks are then assessed for intersections with the pixel plane edges to filter out the tracks that do not traverse the entire sensor thickness. Furthermore, a small percentage of the pixels in the vicinity of the pixel plane are disregarded from the tracks due to substantial errors in drift time measurement in that area. A demonstration of the aforementioned track selection process using the data collected from the Timepix3 detector with a 1 mm CdTe sensor and applied bias voltage of -400 V is illustrated in Fig. 1.

Following the identification of linear tracks within the data, the interaction depth for each pixel along the tracks is reconstructed based on the sensor geometry. The reconstruction method proposed by Bergmann et al [43] is employed for this purpose. Initially, the entry point  $\mathbf{P}_{\text{entry}} = (x_{\text{entry}}, y_{\text{entry}})$  at  $z = 0$  and the exit point  $\mathbf{P}_{\text{exit}} = (x_{\text{exit}}, y_{\text{exit}})$  at  $z = d$  are determined for each track. Subsequently, the interaction depth of each pixel  $\mathbf{P}$  in the track can be computed with

$$z_{\text{geo}}(\mathbf{P}) = \frac{d}{L_{\text{proj}}} \cdot r(\mathbf{P}), \quad (3)$$

where  $d$  is the thickness of the sensor,  $L_{\text{proj}} = |\mathbf{P}_{\text{exit}} - \mathbf{P}_{\text{entry}}|$  is the projected length of the track and  $r(\mathbf{P}) = |\mathbf{P} - \mathbf{P}_{\text{entry}}|$  is the projected distance from the pixel  $\mathbf{P}$  to the entry point. Finally, the correlation between the interaction depth and drift time is derived from the reconstructed tracks and then fitted with Eq. (2) to obtain the electric field parameters.

In fully depleted detectors with sensor materials such as silicon and CdTe, the internal electric field typically exhibits a linear decay from the pixel electrode to the non-collecting electrode. In the case of fully depleted silicon sensors, the electric field can be characterized by [45]

$$E(z) = \left( \frac{U_B}{d} + \frac{U_D}{d^2} \left( \frac{d}{2} - z \right) \right), \quad (4)$$

with  $U_B$  being the applied bias voltage and  $U_D$  being the depletion voltage of the sensor. On the other hand, the electric field in CdTe sensor can be fitted with [43]

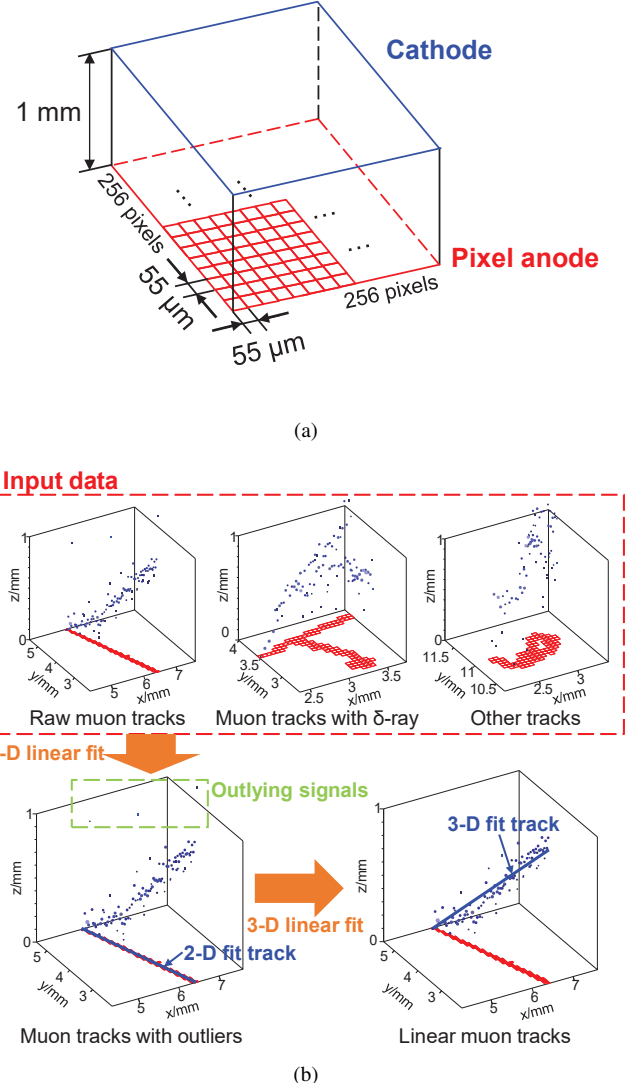


Fig. 1. (Color online) A demonstration of the muon track selection. (a) A diagram of the internal structure of the detector used for the demonstration. (b) Schematic of the muon track selection process. The pixel signals with 3-dimensional position information are marked in blue dots with the corresponding triggered pixels marked in red frames in the pixel plane. The linear muon tracks are picked out via 2-dimensional linear fit (marked with blue line), followed by a 3-dimensional linear fit to exclude the outlying pixel signals.

$$E(z) = -\frac{U_B}{d} \left( 1 + \left( f_1 + \frac{f_2}{U_B} \right) \frac{z}{d} \right), \quad (5)$$

where  $f_1$  and  $f_2$  are the fitting parameters of the model. In this study, we employ the CdTe sensor as a representative example to illustrate the procedure of fitting and extracting the electric field parameters. Combining Eq. (2) and Eq. (5) yields

$$t_0(z_0) = -\frac{d^2}{\mu_e U_B (f_1 + f_2/U_B)} \cdot \ln \left( \frac{(f_1 + f_2/U_B)z_0}{d} + 1 \right), \quad (6)$$

which can be used to perform the fit. In the context of the CdTe sensor where electrons are the collected charge carriers, the mobility  $\mu$  is substituted with the electron mobility  $\mu_e$  in Eq. (6). However, for the detectors that are unable to register signals from the non-collecting electrode, determining the absolute drift time for each pixel becomes challenging. Instead, the drift time is derived by subtracting the recorded time-of-arrival (ToA) of the entry point from the ToA of each pixel. This approach may introduce a systematic error in the calculated drift times as the ToA measurement is significantly influenced by the non-collecting charge carriers (holes in the case of CdTe sensors) near the pixel electrode. To address this, a correction term  $t_{\text{err}}$  is introduced to Eq. (6) to factor in the systematic error of ToA. The adjusted fit function is then derived by rearranging Eq. (6),

$$z_0(t_0) = \frac{d}{f_1 + f_2/U_B} \left( \exp \left( -\frac{\mu_e U_B}{d^2} \right) \cdot (f_1 + \frac{f_2}{U_B}) \cdot (t_0 - t_{\text{err}}) \right) - 1. \quad (7)$$

While Eq. (7) offers a satisfactory representation for scenarios involving a linear electric field, it tends to diverge from the measured data in the vicinity of the pixel plane, as detailed in section III. To address this discrepancy, an exponential correction term and a normalization coefficient are introduced to Eq. (5) to account for the deviations observed in the measured electric field

$$E_{\text{corr}}(z) = -C_{\text{norm}} \cdot \frac{U_B}{d} \cdot \left( 1 + \left( f_1 + \frac{f_2}{U_B} \right) \frac{z}{d} + A \exp \left( -\frac{z}{L} \right) \right), \quad (8)$$

with  $C_{\text{norm}}$  being the normalization coefficient,  $A$  and  $L$  being the amplitude and decay length of the exponential term. The fit function representing the relationship between carrier drift time and interaction depth, as denoted by Eq. (6), can be appropriately adjusted in accordance with the introduced modifications,

$$t_0(z_0) = \int_0^{z_0} \frac{dz}{\mu_e E_{\text{corr}}(z)}, \quad (9)$$

and the coefficient  $C_{\text{norm}}$  can be obtained according to the bias voltage of the detector,

$$C_{\text{norm}} = -\frac{U_B}{\int_0^{z_0} E_{\text{corr}}(z) dz}. \quad (10)$$

## B. Offline inspection of per-pixel spectral characteristics

The offline inspection serves the purpose of effectively capturing shifts in the per-pixel spectral characteristics including detector baseline and gain that can be influenced by the irreversible degradation. This process involves two distinct measurements, one to determine the baseline, which requires no additional radioactive sources, and another to assess the detector gain, utilizing easily procurable low-activity sources.

The initial phase of offline inspection involves a baseline scan, which is a well-established detector calibration procedure [46]. This process entails adjusting the threshold level of each pixel in close proximity to the baseline of the detector and recording the trigger count at each threshold value to outline the baseline distribution for each pixel. Subsequently, the average value of the baseline distribution indicates the baseline level of the corresponding pixel, and the standard deviation reflects the electronic noise present.

The following aspect of the offline inspection focuses on evaluating the detector gain to evaluate both the average gain of the detector and the gain consistency across various areas on the pixel plane. In addition to potential decrease in the overall detector gain, local reductions in the detector gain may also arise from aging effects. This local reduction can lead to significant gain discrepancies among different areas of the pixel plane. This spatial disparity can contribute to the degradation in the energy resolution of the detector, which further underscores the importance of regular assessments of spatial uniformity. Conventional gain evaluation method typically involves using radiation apparatus such as X-ray devices to generate low-energy photons (typically below 30 keV). These photons produce signals confined to a single detector pixel, enabling per-pixel of gain calibration [47]. In contrast, our method only utilizes simple radioactive sources like low-activity (<sup>241</sup>Am positioned adjacent to the non-collecting electrode for data collection. As the charge signal from the radioactive sources can spread across multiple pixels, the data analysis involves segmenting the detector into distinct regions, each containing one or a few pixels, and the size of each region determined by the average size of the full-energy events. To ensure accurate gain estimation for each region, data acquisition is conducted over a specific timeframe to gather sufficient data points per region. Subsequently, the spectrum collected from each region  $i$  is fitted with a Gaussian function to determine the center position  $\mu_i$  of the full-energy peak. Ultimately, the average peak position  $\bar{\mu}$  across all regions is computed, and the relative gain of each region is calculated with

$$G_i = \frac{\mu_i}{\bar{\mu}}. \quad (11)$$

## III. RESULTS AND DISCUSSION

The proposed performance monitoring methodology is tested on a MiniPIX TPX3 detector equipped with a 1 mm thick CdTe sensor. The parameters associated with the charge

311 collection process, detector baseline, and detector gain are  
 312 determined through real-time monitoring and offline inspection  
 313 processes, respectively, utilizing only a single additional  
 314  $^{241}\text{Am}$  source. Variations in the parameters associated with  
 315 the charge collection process are showcased through data ac-  
 316 quired from two 20-hour measurements employing the real-  
 317 time monitoring techniques. The baseline level and electronic  
 318 noise characteristics of each pixel are extracted from the base-  
 319 line scan, while the assessment of overall detector gain and  
 320 gain uniformity is based on the measurements performed with  
 321 the  $^{241}\text{Am}$  source.

322

### 323 A. Real-time monitoring of charge collection process

324 The real-time monitoring process involves utilizing data  
 325 from two sequential measurements, both performed at a de-  
 326 tector bias voltage of -400 V. Initially, the Timepix3 detec-  
 327 tor is exposed to cosmic muons for 20 hours to gather data  
 328 (referred to as “measurement 1”). Since the detector has  
 329 been operating for several consecutive days before this mea-  
 330 surement, with the average temperature of the sensor reaching  
 331 around 35 °C, a 30-minute cool-down period is initiated  
 332 by switching off the detector after measurement 1. Subse-  
 333 quently, another 20-hour data collection session (referred to  
 334 as “measurement 2”) is conducted, with the sensor operat-  
 335 ing at approximately 25 °C. Despite the absence of external  
 336 temperature regulation during the measurements, the metal  
 337 casing surrounding the detector, combined with passive cool-  
 338 ing measures, was sufficient to mitigate abrupt temperature  
 339 changes in the sensor. Muon tracks are selected from the  
 340 datasets, and the correlations between charge carrier drift time  
 341 and interaction depth are fitted with Eq. (9) for each set of  
 342 data. As illustrated in Fig. 2, the fitting results exhibit discrep-  
 343 ancies in charge carrier drift time between the two measure-  
 344 ments. To further investigate the underlying reasons for these  
 345 disparities, the internal electric field distribution and electron  
 346 mobility are derived using Eqs. (8) and (10). Fig. 3 show-  
 347 cases the derived electric field distributions for measurements  
 348 1 and 2, with the fitted values of the parameters from Eqs. (8)  
 349 and (10) given in table 1. It is evident that the electric field of  
 350 the two measurements remain consistent despite the notable  
 351 fitting error in measurement 1, which suggests that the impact  
 352 of polarization in the sensor material is negligible. However,  
 353 there is a significant variance in electron mobilities between  
 354 the two measurements. Given that measurement 1 is con-  
 355 ducted at a higher average temperature (~35 °C) compared  
 356 to measurement 2 (~25 °C), the variation in electron mobil-  
 357 ity is most likely attributed to this temperature differential.  
 358 To address this, we extrapolated the electron mobility under  
 359 the condition of measurement 2 using the mobility derived  
 360 from measurement 1 and the theoretical electron mobility of  
 361 CdTe [48], which is also shown in table 1. The close agree-  
 362 ment between the measured and estimated electron mobilities  
 363 in measurement 1 confirms that the alternations in the charge  
 364 collection process is primarily caused by temperature fluctu-  
 365 ations. In practical applications, this monitoring procedure

366 can be employed to regularly monitor variations in the op-  
 367 erational conditions such as the ambient temperature. Upon  
 368 detecting such changes, appropriate measures such as stabi-  
 369 lizing the sensor temperature can be taken to maintain the data  
 370 integrity.

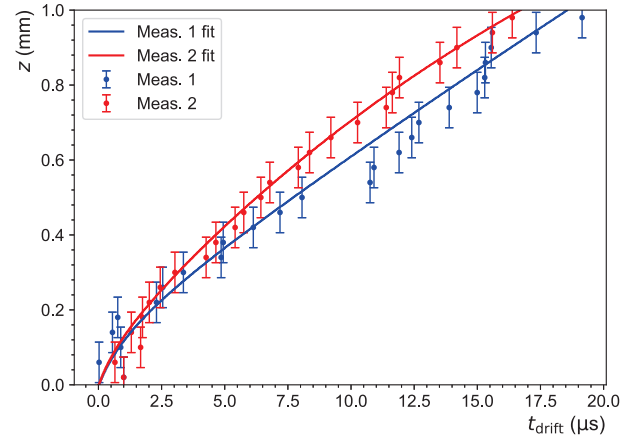


Fig. 2. (Color online) The correlation between carrier drift time and depth extracted from measurements 1 and 2, along with the fitting results.

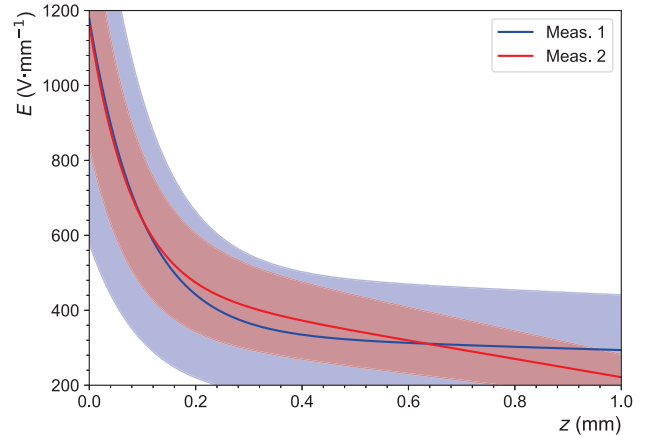


Fig. 3. (Color online) The electric field distribution calculated from the data of measurements 1 and 2.

371

### 372 B. Offline inspection of per-pixel spectral characteristics

373 The initial phase of the offline inspection involves con-  
 374 ducting a baseline scan as described in subsection II B with  
 375 the bias voltage set at -400 V. Following the acquisition of  
 376 baseline distributions from the scan data, the per-pixel base-  
 377 line level and electronic noise distribution are determined

TABLE 1. Fitted values of the operating parameters related to the charge collection process derived from measurements 1 and 2. Note that the estimated electron mobility of measurement 1 is calculated according to the result of measurement 2 and theoretical values [48].

Parameters	Result of measurement 1	Result of measurement 2
Temperature ( $^{\circ}\text{C}$ )	$\sim 35$	$\sim 25$
Electron mobility $\mu_e$ ( $\text{m}^2 \cdot \text{V}^{-1} \cdot \text{s}^{-1}$ )	$15.09 \pm 2.14$	$17.23 \pm 1.29$
Estimated electron mobility $\mu_{e,\text{est}}$ ( $\text{m}^2 \cdot \text{V}^{-1} \cdot \text{s}^{-1}$ )	$16.69 \pm 1.25$	–
$f_1 + f_2/U_B$	$-0.13 \pm 0.25$	$-0.52 \pm 0.06$
$A$	$2.17 \pm 5.31$	$1.55 \pm 2.71$
$L$ ( $\mu\text{m}$ )	$86.9 \pm 95.5$	$80.9 \pm 62.8$
$C_{\text{norm}}$	$0.84 \pm 0.42$	$1.16 \pm 0.32$

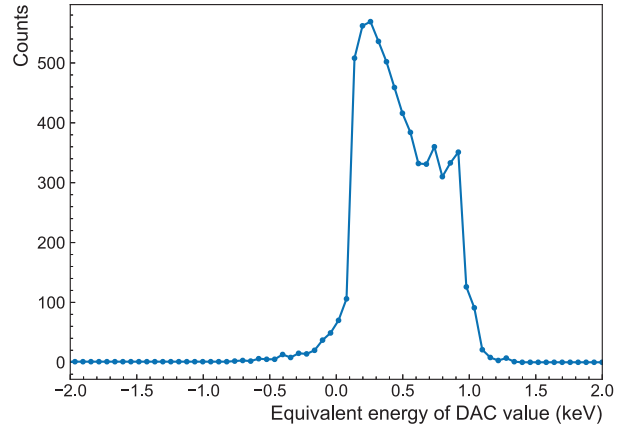


Fig. 4. (Color online) Demonstration of the baseline distribution derived from the baseline scan data from one pixel of the detector.

378 by the center and standard deviation of the baseline distribution of the corresponding pixel, as depicted in Fig. 4. It  
379 should be noted that the baseline level is determined by  
380 adjusting the output of the digital to analog converter (DAC)  
381 that regulates the threshold. Thus, the baseline levels are  
382 quantified in equivalent energy values derived from the DAC  
383 output values according to the energy calibration param-  
384 eters. Fig. 5 displays the resultant per-pixel baseline and  
385 noise distribution which indicates an average baseline value  
386 of  $E_b = (0.218 \pm 0.095)$  keV. Since the average detector  
387 baseline level was initially aligned to the equivalent energy  
388 of 0 keV during the energy calibration process of the factory  
389 test conducted under identical conditions, it is evident that  
390 the baseline of the detector has drifted from the calibrated  
391 values after 3 years of operation, in which the detector was  
392 irradiated with mostly gamma-ray photons with an accum-  
393 lated flux of  $\sim 3.19 \times 10^9 \text{ cm}^{-2}$ . This rise in baseline level is  
394 most likely attributed to the increase in leakage current, which  
395 is most likely caused by aging effects. It signals a potential  
396 need for recalibration of the per-pixel energy response, which  
397 includes aligning the threshold DAC and the signal amplitude  
398 with the deposited energy. Additionally, the result provides  
399 a possible explanation to the deviation of the baseline distri-  
400 bution depicted in Fig. 4 from a standard Gaussian distribu-  
401 tion. This deviation may stem from the response of the detec-  
402 tor's preamplifier to signals of different polarities at increased  
403 baseline levels [46].

405 The subsequent segment of the offline inspection involves  
406 the assessment of detector gain. This procedure is carried out  
407 by exposing the detector to the 60 keV gamma rays of an  
408  $^{241}\text{Am}$  source placed at the incident window (cathode side)  
409 of the detector. Given the relatively low activity level (tens  
410 of  $\mu\text{Ci}$ ) of the  $^{241}\text{Am}$  source, it is necessary for the mea-  
411 surement to last a prolonged period of 48 hours in order to  
412 accumulate an adequate amount of data to form the energy  
413 spectrum of each region. The bias voltage of the detector is  
414 set to -300 V. Based on the average event sizes in both x and  
415 y directions of the pixel plane, each region is configured to  
416 encompass  $2 \times 2$  pixels. A depiction of the energy spec-  
417 trum in one of the consequent  $128 \times 128$  regions is shown  
418 in Fig. 6. The spectra are fitted using Gaussian functions,

419 and the fitted centers of the Gaussian peak indicate the gain  
420 in the corresponding regions. In order to evaluate the gain  
421 variation following 3 years of operation, a set of data col-  
422 lected under identical operating conditions is analysed using  
423 the same approach. After subtracting the per-pixel baseline  
424 level to accommodate the increase in baseline, the spectra of  
425 the 60 keV peak obtained in the current measurement (Dec.  
426 2023) and 3 years prior (Sep. 2020) are compared in Fig. 7.  
427 The result indicates an evident decrease in detector gain that  
428 is likely caused by aging effects, which leads to the reduc-  
429 tion in CCE. This shift in detector gain also necessitates the  
430 recalibration of the per-pixel energy response to ensure the  
431 correctness of the measured energy values. Furthermore, by  
432 normalizing the regional gain distribution with Eq. (11), the  
433 spatial gain uniformity is determined for both data and the  
434 results are showcased in Figs. 8(a) and 8(b). The compari-  
435 son between the two figures reveals a decrease in local gain  
436 across several regions. Besides, a discernible pattern can be  
437 found in Fig. 8, which exhibits strong consistency between  
438 the two figures. This spatial distribution pattern in local gain  
439 has been reported in previous studies [47], which reported  
440 that it can result from calibration imperfections and sensor  
441 inhomogeneity. The spatial inhomogeneity of detector gain  
442 can be mitigated through per-pixel gain correction, utilizing  
443 the relative gain distribution derived from the gain assessment  
444 process.

#### IV. CONCLUSION

446 In this article, we introduce a new, cost-effective monitor-  
447 ing approach based on existing methodologies for semicon-  
448 ductor pixel detectors in long-term operations. This method  
449 combines the real-time monitoring to monitor the charge car-  
450 rier drift process, which can be influenced by temporary ef-  
451 fects, and the offline inspection to assess the per-pixel spectral  
452 characteristics including detector baseline and gain variations  
453 resulting from irreversible performance degradation. To val-  
454 idate the procedure, the real-time monitoring and offline in-

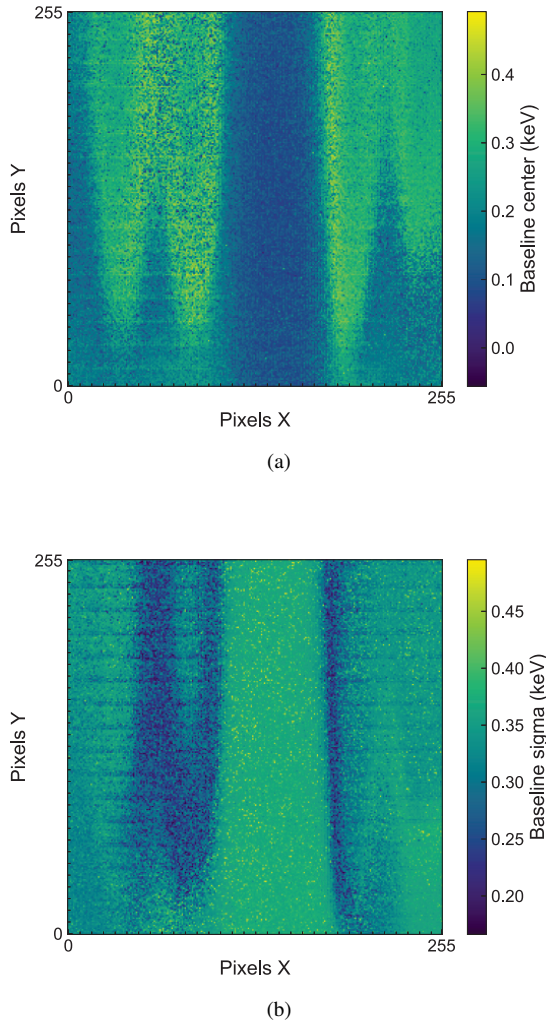


Fig. 5. (Color online) The baseline centers (a) and standard deviations (b) extracted from the baseline scan data via Gaussian fitting.

455 spections were conducted on a Timepix3 detector featuring a  
 456 1 mm-thick CdTe sensor. Results from real-time monitoring  
 457 revealed shifts in the carrier drifting parameters due to tem-  
 458 perature fluctuations. In practice, appropriate measures such  
 459 as temperature stabilization need to be taken once such varia-  
 460 tions are identified. On the other hand, the offline inspection  
 461 uncovered a rise in the detector baseline, a decrease in the  
 462 detector gain and changes in spatial irregularities in per-pixel  
 463 gain. These fluctuations in detector performance due to irre-  
 464 versible degradation indicates the necessity for recalibrations  
 465 such as per-pixel energy calibration and corrections like spa-  
 466 tial gain uniformity correction to be implemented. In conclu-  
 467 sion, the aforementioned findings confirm the effectiveness of  
 468 the proposed monitoring procedure in monitoring the perfor-

469 mance of pixel detectors.

470 While the monitoring procedure demonstrated effective-  
 471 ness in detecting changes in CdTe pixel detectors, further val-  
 472 idation on detectors with different sensor materials like sili-

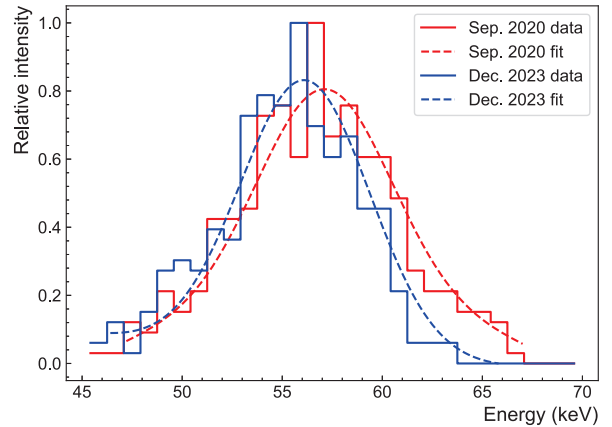


Fig. 6. (Color online) Depiction of the energy spectra of the 60 keV gamma rays from the  $^{241}\text{Am}$  source in one of the  $2 \times 2$ -pixel regions collected in Sep. 2020 and Dec. 2023 with the corresponding Gaussian fitting results.

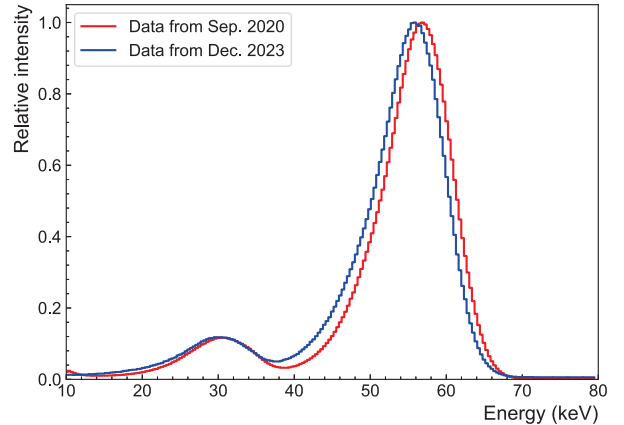


Fig. 7. (Color online) Comparison between the energy spectra of the 60 keV gamma rays from  $^{241}\text{Am}$  source collected in Sep. 2020 and Dec. 2023.

473 con is warranted. Additionally, testing under actual long-term  
 474 operational conditions, including aging tests and exposure to  
 475 high-flux particle beams, is essential. After rigorous test-  
 476 ing and refinement based on the test results, the monitoring  
 477 procedure can be applied in fields requiring long-term opera-  
 478 tions. Such procedure offers a cost-efficient approach to reg-  
 479 ularly monitor detector performance, especially in industrial  
 480 and medical applications with numerous detectors.

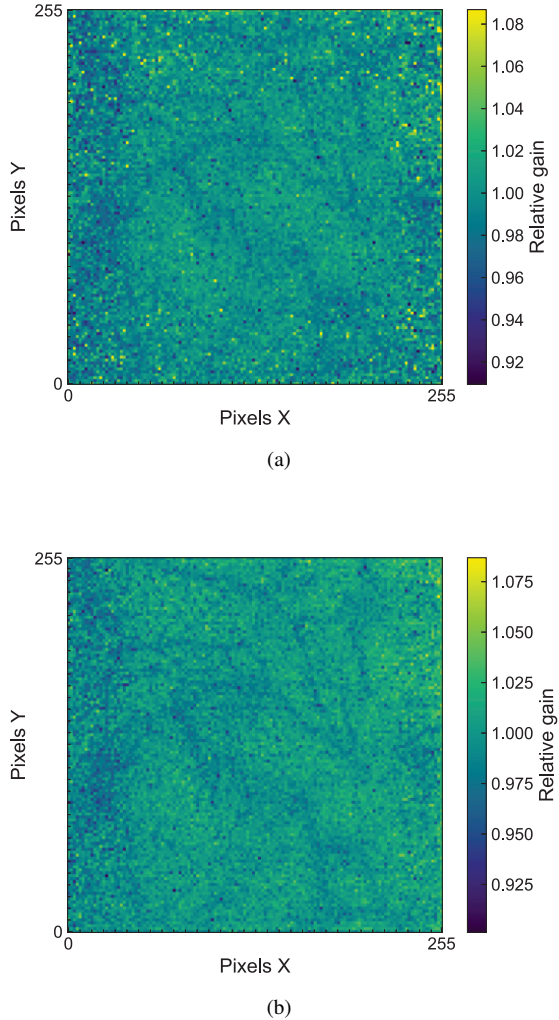


Fig. 8. (Color online) Comparison between the spatial gain uniformity derived from the measurement with the 60 keV gamma rays from  $^{241}\text{Am}$  source collected in (a) Sep. 2020 and (b) Dec. 2023.

- 
- 481 [1] D. Turecek, J. Jakubek, E. Trojanova et al., Application of 497  
482 Timepix3 based CdTe spectral sensitive photon counting 498  
483 detector for PET imaging. Nucl. Instrum. Methods Phys. Res. A 499  
484 **895**, 84–89 (2018). doi: [10.1016/j.nima.2018.04.007](https://doi.org/10.1016/j.nima.2018.04.007)  
485 [2] Z.H. Xie, S.Y. Li, K. Yang et al., Evaluation of a wobbling 500  
486 method applied to correcting defective pixels of CZT detectors 501  
487 in SPECT imaging. Sens. Switz. **16**, 772 (2016). doi: 502  
[10.3390/s16060772](https://doi.org/10.3390/s16060772)  
488 [3] T. Wei, H. Yang, Z. Deng et al., Design and evaluation of EM- 503  
489 PIX2, a 100 kfps, high dynamic range pixel detector readout 504  
490 ASIC for electron microscopy. J. Instrum. **18**, C12007 (2023). 505  
491 doi: [10.1088/1748-0221/18/12/C12007](https://doi.org/10.1088/1748-0221/18/12/C12007)  
492 [4] Y. Auad, J. Baaboura, J.-D. Blazit et al., Time calibration 506  
493 studies for the Timepix3 hybrid pixel detector in electron 507  
494 microscopy. Ultramicroscopy **257**, 113889 (2024). doi: 508  
495 [10.1016/j.ultramic.2023.113889](https://doi.org/10.1016/j.ultramic.2023.113889)  
496 [5] J. Jakubek, C. Granja, O. Jakel et al., Detection and track visualization of primary and secondary radiation in hadron therapy beams with the pixel detector Timepix. Paper presented at IEEE Nuclear Science Symposium & Medical Imaging Conference, Knoxville, TN, USA, 30 October - 06 November, 2010. doi: [10.1109/NSSMIC.2010.5874118](https://doi.org/10.1109/NSSMIC.2010.5874118)  
497 [6] M. Metzner, D. Zhevachevska, A. Schlechter et al., Energy painting: helium-beam radiography with thin detectors and multiple beam energies. Phys. Med. Biol. **69**, 055002 (2024). doi: [10.1088/1361-6560/ad247e](https://doi.org/10.1088/1361-6560/ad247e)  
498 [7] J. Liu, M. Barbero, J.B.D. Mendizabal, et al. Performance 509  
499 of radiation-hard HV/HR CMOS sensors for the ATLAS inner 510  
500 detector upgrades. J. Instrum. **11**, C03044 (2016). doi: 511  
[10.1088/1748-0221/11/03/C03044](https://doi.org/10.1088/1748-0221/11/03/C03044)  
501 [8] M. Schwenke, K. Zuber, B. Janutta et al., Exploration of Pixelated detectors for double beta decay searches within the CO-  
502

- 513 BRA experiment. *Nucl. Instrum. Methods Phys. Res. A* **650**,  
 514 73–78 (2011). doi: [10.1016/j.nima.2010.12.128](https://doi.org/10.1016/j.nima.2010.12.128)
- 515 [9] J. Prince, D. Hargrove, A. Carpenter et al., Development and  
 516 performance of CMOS scientific camera platform used at the  
 517 National Ignition Facility. Paper presented at SPIE Optical En-  
 518 gineering + Applications, San Diego, CA, USA, 28 July, 2023.  
 519 doi: [10.1117/12.2675561](https://doi.org/10.1117/12.2675561)
- 520 [10] B. Hong, G.Q. Zhong, L.Q. Hu, et al., Diagnostic of  
 521 Fusion Neutrons on EAST Tokamak Using 4H-SiC De-  
 522 tector. *IEEE Trans. Nucl. Sci.* **69**, 639–644 (2022). doi:  
 523 [10.1109/TNS.2022.3146180](https://doi.org/10.1109/TNS.2022.3146180)
- 524 [11] Y.P. Zhang, Y. Liu, J.W. Yang, et al., A new soft x-ray pulse  
 525 height analysis array in the HL-2A tokamak. *Rev. Sci. Instrum.*  
 526 **80**, 126104 (2009). doi: [10.1063/1.3263910](https://doi.org/10.1063/1.3263910)
- 527 [12] G. Pausch, J. Berthold, W. Enghardt, et al., Detection systems  
 528 for range monitoring in proton therapy: Needs and challenges.  
 529 *Nucl. Instrum. Methods Phys. Res. A* **954**, 161227 (2020). doi:  
 530 [10.1016/j.nima.2018.09.062](https://doi.org/10.1016/j.nima.2018.09.062)
- 531 [13] X. Zhang, S.Y. Bao, M.Z. Wang et al., Stability and accuracy  
 532 of fat quantification on photon-counting detector CT with var-  
 533 ious scan settings. *Eur. J. Radiol.* **177**, 111545 (2024). doi:  
 534 [10.1016/j.ejrad.2024.111545](https://doi.org/10.1016/j.ejrad.2024.111545)
- 535 [14] D. Zhao, R.L. Gao, W. Cheng et al., Heavy-to-light electron  
 536 transition enabling real-time spectra detection of charged par-  
 537 ticles by a biocompatible semiconductor. *Nat. Commun.* **15**,  
 538 1115 (2024). doi: [10.1038/s41467-024-45089-2](https://doi.org/10.1038/s41467-024-45089-2)
- 539 [15] Y. Lin, H.Q. Zhang, S.Z. Gu et al., Proton beam spot  
 540 size and position measurements using a multi-strip ion-  
 541 ization chamber. *Physica Med.* **123**, 103411 (2024). doi:  
 542 [10.1016/j.ejmp.2024.103411](https://doi.org/10.1016/j.ejmp.2024.103411)
- 543 [16] R. Quay, C. Moglestue, V. Palankovski et al., A temperature  
 544 dependent model for the saturation velocity in semiconductor  
 545 materials. *Mater. Sci. Semicond. Process.* **3**, 149–155 (2000).  
 546 doi: [10.1016/S1369-8001\(00\)00015-9](https://doi.org/10.1016/S1369-8001(00)00015-9)
- 547 [17] J. Xu, M. Shur, Temperature dependence of electron mobility  
 548 and peak velocity in compensated GaAs. *Appl. Phys. Lett.* **52**,  
 549 922–923 (1988). doi: [10.1063/1.199274](https://doi.org/10.1063/1.199274)
- 550 [18] Z. Li, Radiation damage effects in Si materials and detectors  
 551 and rad-hard Si detectors for SLHC. *J. Instrum.* **4**, P03011  
 552 (2009). doi: [10.1088/1748-0221/4/03/P03011](https://doi.org/10.1088/1748-0221/4/03/P03011)
- 553 [19] L. Zhang, Y. Gu, J. Ma et al., CLeakage Performance  
 554 of 4H-SiC CMOS Logic Circuits after Gamma Irradia-  
 555 tion. *IEEE Electron Device Lett.* **45**, 542–545 (2024). doi:  
 556 [10.1109/LED.2024.3368527](https://doi.org/10.1109/LED.2024.3368527)
- 557 [20] A.I. Kondrik, Mechanisms of degradation of the detecting  
 558 properties of cdte and cdznte under gamma radiation exposure.  
 559 *East Eur. J. Phys.* **2021**, 116–123 (2021). doi: [10.26565/2312-4334-2021-3-18](https://doi.org/10.26565/2312-4334-2021-3-18)
- 560 [21] S.R. Li, G. De Geronimo, W. Chen et al., A low-power,  
 561 radiation-resistant ASIC for SDD-based X-ray spectrome-  
 562 ters. *IEEE Trans. Nucl. Sci.* **60**, 3057–3062 (2013). doi:  
 563 [10.1109/TNS.2013.2268980](https://doi.org/10.1109/TNS.2013.2268980)
- 564 [22] M. Aaboud, G. Aad, B. Abbott et al., Modelling radiation dam-  
 565 age to pixel sensors in the ATLAS detector. *J. Instrum.* **14**,  
 566 P06012 (2019). doi: [10.1088/1748-0221/14/06/P06012](https://doi.org/10.1088/1748-0221/14/06/P06012)
- 567 [23] L. Bao, G.Q. Zha, Y.X. Gu et al., Study on radiation damage  
 568 effects on CdZnTe detectors under 3 MeV and 2.08 GeV Kr  
 569 ion irradiation. *Mater. Sci. Semicond. Process.* **121**, 105369  
 570 (2021). doi: [10.1016/j.mssp.2020.105369](https://doi.org/10.1016/j.mssp.2020.105369)
- 571 [24] L.Y. Xu, W.Q. Jie, G.Q. Zha et al., Radiation damage on  
 572 CdZnTe:In crystals under high dose 60Co  $\gamma$ -rays. *Cryst. Eng.*  
 573 *Comm.* **15**, 10304–10310 (2013). doi: [10.1039/c3ce41734d](https://doi.org/10.1039/c3ce41734d)
- 574 [25] Y.X. Gu, W.Q. Jie, C.C. Rong et al., Study on the bias-  
 575 dependent effects of proton-induced damage in CdZnTe radia-  
 576 tion detectors using ion beam induced charge microscopy. *Mi-*  
 577 *cron*, **88**, 54–59 (2016). doi: [10.1016/j.micron.2016.06.003](https://doi.org/10.1016/j.micron.2016.06.003)
- 578 [26] R.R. Guo, Y.D. Xu, T. Wang et al., An analysis of defects in-  
 579 duced by high dose  $\gamma$ -ray irradiation and their influence on the  
 580 charge transport properties in CdZnTe detectors. *J. Appl. Phys.*  
 581 **127**, 024501 (2020). doi: [10.1063/1.5126792](https://doi.org/10.1063/1.5126792)
- 582 [27] A. Šagátová, B. Zátko, F. Dubecký et al., Radiation  
 583 hardness of GaAs sensors against gamma-rays, neutrons  
 584 and electrons. *Appl. Surf. Sci.* **395**, 66–71 (2017). doi:  
 585 [10.1016/j.apsusc.2016.08.167](https://doi.org/10.1016/j.apsusc.2016.08.167)
- 586 [28] F. Nava, P. Vanni, C. Canali et al., Evidence for plasma ef-  
 587 fect on charge collection efficiency in proton irradiated GaAs  
 588 detectors. *Nucl. Instrum. Methods Phys. Res. A* **426**, 185–191  
 589 (1999). doi: [10.1016/S0168-9002\(98\)01490-9](https://doi.org/10.1016/S0168-9002(98)01490-9)
- 590 [29] J.B. Peng, J.J. Zou, B. Tang et al., Effects of electron ir-  
 591 radation and thermal annealing on characteristics of semi-  
 592 insulating gallium-arsenide alpha-particle detectors. *Nucl. In-*  
 593 *strum. Methods Phys. Res. A* **969**, 164017 (2020). doi:  
 594 [10.1016/j.nima.2020.164017](https://doi.org/10.1016/j.nima.2020.164017)
- 595 [30] W.Y. Ma, L.Y. Liu, R.L. Gao et al., Radiation hardness char-  
 596 acteristics of self-powered detector based on SiC/Si hetero-  
 597 junction diode. *Sens. Actuators Phys.* **361**, 114563 (2023). doi:  
 598 [10.1016/j.sna.2023.114563](https://doi.org/10.1016/j.sna.2023.114563)
- 599 [31] J. Liu, Y. Liu, S. Fang et al., Circuit design of a novel front  
 600 readout circuit for SiC neutron detector with leakage current  
 601 compensation. *J. Phys.: Conf. Ser.* **2740**, 012033 (2024). doi:  
 602 [10.1088/1742-6596/2740/1/012033](https://doi.org/10.1088/1742-6596/2740/1/012033)
- 603 [32] K.F. Qin, L.J. Wang, J.H. Min et al., Effects of contact interface  
 604 degradation on the performance of CdZnTe detectors. *Vacuum*  
 605 **86**, 943–945 (2012). doi: [10.1016/j.vacuum.2011.07.048](https://doi.org/10.1016/j.vacuum.2011.07.048)
- 606 [33] M.D. Wilson, P. Barnes, R.C. Cernik et al., Comparison of the  
 607 X-ray performance of small pixel CdTe and CZT detectors. Pa-  
 608 per presented at IEEE Nuclear Science Symposium & Medical  
 609 Imaging Conference, Knoxville, TN, USA, 30 October - 06  
 610 November, 2010. doi: [10.1109/NSSMIC.2010.5874554](https://doi.org/10.1109/NSSMIC.2010.5874554)
- 611 [34] A. Meuris, O. Limousin, C. Blondel et al., Characterization of  
 612 polarization phenomenon in Al-Schottky CdTe detectors using  
 613 a spectroscopic analysis method. *Nucl. Instrum. Methods Phys.*  
 614 *Res. A* **654**, 293–299 (2011). doi: [10.1016/j.nima.2011.05.084](https://doi.org/10.1016/j.nima.2011.05.084)
- 615 [35] M. Daniel, M. Danielsson, B.D. Yanoff et al., Charge collec-  
 616 tion efficiency of CdTe detectors. Paper presented at Progress  
 617 in Biomedical Optics and Imaging – Proceedings of SPIE, San  
 618 Diego, CA, USA, 7 April, 2023. doi: [10.1117/12.2653872](https://doi.org/10.1117/12.2653872)
- 619 [36] S. Yin, T.O. Tümer, D. Maeding et al., Direct conver-  
 620 sion CdZnTe and CdTe detectors for digital mammogra-  
 621 phy. *IEEE Trans. Nucl. Sci.* **49**, 176–181 (2002). doi:  
 622 [10.1109/TNS.2002.998748](https://doi.org/10.1109/TNS.2002.998748)
- 623 [37] J. Fink, H. Krüger, P. Lodomez et al., Characterization of  
 624 charge collection in CdTe and CZT using the transient current  
 625 technique. *Nucl. Instrum. Methods Phys. Res. A* **560**, 435–443  
 626 (2006). doi: [10.1016/j.nima.2006.01.072](https://doi.org/10.1016/j.nima.2006.01.072)
- 627 [38] X.Z. Wang, T. Wei, Z. Deng, , Experimental characteriza-  
 628 tion of an X-ray photon counting detector. *J. Instrum.* **17**, C07005  
 629 (2022). doi: [10.1088/1748-0221/17/07/C07005](https://doi.org/10.1088/1748-0221/17/07/C07005)
- 630 [39] F. Principato, A.A. Turturici, M. Gallo et al., Polariza-  
 631 tion phenomena in Al/p-CdTe/Pt X-ray detectors. *Nucl. In-*  
 632 *strum. Methods Phys. Res. A* **730**, 141–145 (2013). doi:  
 633 [10.1016/j.nima.2013.05.157](https://doi.org/10.1016/j.nima.2013.05.157)
- 634 [40] A. Cola, I. Farella, N. Auricchio et al., Investigation of the elec-  
 635 tric field distribution in x-ray detectors by Pockels effect. *J.*  
 636 *Opt. A* **8**, S467–S472 (2006). doi: [10.1088/1464-4258/8/7/S24](https://doi.org/10.1088/1464-4258/8/7/S24)
- 637 [41] A. Cola, L. Dominici, A. Valletta, Electric-Field Mapping of

- 639 Optically Perturbed CdTe Radiation Detectors. *Sens.* **23**, 4795  
 640 (2023). doi: [10.3390/s23104795](https://doi.org/10.3390/s23104795)
- 641 [42] C. Canali, M. Martini, G. Ottaviani et al., Transport properties  
 642 of CdTe. *Phys. Rev. B* **4**, 422–431 (1971). doi: [10.1103/Phys-  
 643 RevB.4.422](https://doi.org/10.1103/PhysRevB.4.422)
- 644 [43] B. Bergmann, P. Burian, P. Manek et al., 3D reconstruction of  
 645 particle tracks in a 2 mm thick CdTe hybrid pixel detector. *Eur. Phys. J. C* **79**, 165 (2019). doi: [10.1140/epjc/s10052-019-6673-  
 646 z](https://doi.org/10.1140/epjc/s10052-019-6673-z)
- 647 [44] J.X. Wen, X.T. Zheng, H.Z. Gao et al., Optimization of  
 648 Timepix3-based conventional Compton camera using electron  
 649 track algorithm. *Nucl. Instrum. Methods Phys. Res. A* **1021**,  
 650 165954 (2022). doi: [10.1016/j.nima.2021.165954](https://doi.org/10.1016/j.nima.2021.165954)
- 651 [45] J. Durst, Modelling and Simulation of Pixelated Photon  
 652 Counting X-ray Detectors for Imaging. Friedrich-Alexander-  
 653 Universitaet Erlangen-Nuernberg, 2008
- 654 [46] M. Gaspari, J. Alozy, R. Ballabriga et al., Design of the analog  
 655 front-end for the Timepix3 and Smallpix hybrid pixel detectors  
 656 in 130 nm CMOS technology. *J. Instrum.* **9**, C01037–C01037  
 657 (2014). doi: [10.1088/1748-0221/9/01/C01037](https://doi.org/10.1088/1748-0221/9/01/C01037)
- 658 [47] S. Fernandez-Perez, V. Boccone, C. Broennimann et al., Char-  
 659 acterization of a hybrid pixel counting detector using a sil-  
 660 icon sensor and the IBEX readout ASIC for electron de-  
 661 tection. *J. Instrum.* **16**, P10034 (2021). doi: [10.1088/1748-  
 662 0221/16/10/P10034](https://doi.org/10.1088/1748-0221/16/10/P10034)
- 663 [48] K. Suzuki, S. Seto, T. Sawada et al., Carrier transport properties  
 664 of HPB CdZnTe and THM CdTe:Cl. *IEEE Trans. Nucl. Sci.* **49**,  
 665 1287–1291 (2002). doi: [10.1109/TNS.2002.1039653](https://doi.org/10.1109/TNS.2002.1039653)
- 666